Green Chemistry

PAPER

View Article Online
View Journal



Cite this: DOI: 10.1039/d5gc04545b

# *In situ* photocatalytic formation of carbon quantum dots from corn stover *via* interfacial hydrogen peroxide generation

Xuejing Kang,[a] Qian Yang,[b] Sean Xiang Tang,[a] Zhe Chen,[a] Samir Budhathoki,[a] Ramhari Paneru,[a] Soyoung Kim,[g] Yan Bai,[c] Qian Li,[c] Zhongbing Chen,[d] Alexander Goroncy,[e] Richard N. Zare *[f] and Maohong Fan *[g,h]

We present a sustainable photocatalytic approach for synthesizing carbon quantum dots (CQDs) from renewable corn stover under simulated solar irradiation. In this process, hydrogen peroxide ($H_2O_2$) is spontaneously and continuously generated at the gas–water microdroplet interface. Naturally occurring ferrous ($Fe^{2+}$) and other multivalent ions in the corn stover catalyze the decomposition of $H_2O_2$, producing highly reactive hydroxyl radicals (•OH) that drive the oxidation and fragmentation of lignocellulosic components, ultimately leading to CQD formation. An oxygen-rich environment further facilitates the reaction. Compared to conventional methods, this approach enhances $H_2O_2$ utilization efficiency while avoiding excessive oxidation associated with high doses of external oxidants (*e.g.*, $H_2O_2$ and $HNO_3$). The resulting CQDs (4.6 ± 0.8 nm) exhibit intense blue fluorescence with a quantum yield of up to 20.1 ± 0.8%. Structural analyses (XRD, FTIR, Raman, NMR, and XPS) confirm their amorphous graphitic nature with nitrogen self-doping. Uniform CQDs with an average size of 3.1 ± 1.4 nm and high purity were obtained through centrifugation and dialysis purification. This low-cost, scalable method, which integrates *in situ* $H_2O_2$ generation at the microdroplet interface, offers a promising pathway for environmentally friendly CQD production.

Received 29th August 2025,
Accepted 6th March 2026

DOI: 10.1039/d5gc04545b

rsc.li/greenchem



## Green foundation

1. We demonstrate a low-energy, catalyst-free, and renewable feedstock-based strategy to produce high-value nanomaterials, namely carbon quantum dots (CQDs), from agricultural waste (corn stover) using water microdroplets.
2. CQDs of 3–5 nm size with quantum yields of up to 20.1% were produced without strong acids or concentrated oxidants. The method avoids liters of 1–10 M $HNO_3$ or >30% $H_2O_2$ solutions typically required in conventional routes.
3. This work can be made greener and elevated by further research on replacing simulated solar light with direct sunlight, further reducing energy demand, on employing recycled or wastewater streams to minimize freshwater consumption, and by investigating whether residual lignin/cellulose fractions after CQD formation can be valorized, achieving a zero-waste biorefinery model.

## 1. Introduction

Carbon Quantum Dots (CQDs) are carbon-based nanoparticles, typically less than 10 nm in size, renowned for their exceptional optical, electrical, and chemical properties.[1–4] Since their discovery in 2004,[5] CQDs have received much interest because of their diverse applications in bioimaging, drug delivery, environmental sensing, and clean energy production.[6–9] Their intrinsic photoluminescence, chemical stability, and biocompatibility position them as a promising, nontoxic alternative to traditional semiconductor quantum dots, particularly for sustainable applications.[10–13] Moreover, CQDs offer an eco-friendly nanomaterial solution, potentially reducing costs associated with $CO_2$ emission control.[14–16]

[a]Department of Energy & Petroleum Engineering, University of Wyoming, Laramie, WY 82071, USA
[b]Center for Advanced Scientific Instrumentation, University of Wyoming, Laramie, WY 82071, USA
[c]College of Chemistry and Chemical Engineering, Henan University, Kaifeng, Henan 475004, P.R. China
[d]Department of Applied Ecology, Faculty of Environmental Sciences, Czech University of Life Sciences Prague, Kamýcká 129, 16500 Praha-Suchdol, Czech Republic
[e]Department of Chemistry, University of Wyoming, Laramie, WY 82071, USA
[f]Department of Chemistry, Stanford University, Stanford, CA 94305, USA. E-mail: zare@stanford.edu
[g]College of Engineering and Physical Sciences, and School of Energy Resources, University of Wyoming, Laramie, WY 82071, USA. E-mail: mfan@uwyo.edu
[h]College of Engineering, Georgia Institute of Technology, Atlanta, GA 30332, USA

CQDs have been synthesized through top-down methods, such as laser ablation, arc discharge, and electrochemical exfoliation, which break down larger carbon structures, or bottom-up methods, including chemical oxidation, microwave irradiation, hydrothermal, and pyrolysis techniques, which assemble CQDs from molecular precursors.[3,17,18] Conventional carbon sources include graphite and graphene in top-down approaches, and citric acid or glucose in bottom-up approaches. A promising and sustainable alternative involves synthesizing CQDs from renewable agricultural biomass,[19] promoting a circular economy. However, current biomass-based synthesis methods often rely on concentrated acids, strong oxidants (*e.g.*, $H_3PO_4$, $H_2SO_4$, and $HNO_3$), and high-temperature reaction conditions, which limit their environmental and economic viability.

Hydrogen peroxide ($H_2O_2$) is an environmentally friendly oxidizing agent that decomposes into water, making it attractive for various applications, including bleaching, sterilization, and organic reactions.[20] While some studies have employed Fenton reagents (acidic $H_2O_2/Fe^{2+}$–$Fe^{3+}$) or $H_2O_2/W_{18}O_{49}$ systems for carbon nanodot synthesis,[21–23] Zare and colleagues recently demonstrated a novel method for *in situ* $H_2O_2$ generation using mechanical energy-driven microdroplets at water–gas and water–solid interfaces.[24–28]

Although microdroplet chemistry has advanced rapidly, prior studies have centered on pure water or simple dissolved molecules, leaving their potential for the green, low-energy conversion of renewable biomass largely unexplored. Here, we report a facile photocatalytic approach for biomass-derived CQD synthesis utilizing the spontaneous $H_2O$-to-$H_2O_2$ conversion strategy. This method operates without external catalysts, strong oxidants, or acids. Specifically, when corn stover is mixed with deionized water and exposed to simulated sunlight, $H_2O_2$ forms *in situ*, enabling the direct synthesis of CQDs. This environmentally benign process provides a mild, scalable, and sustainable route for producing high-quality CQDs from raw lignocellulosic biomass and establishes a foundation for integrating microdroplet reactivity with solar-driven carbon transformation.

# 2. Methods

## 2.1 Materials

The corn stover was purchased from a research field at the University of Wyoming. Quinine sulfate dihydrate, cellulose, hemicellulose (from *Aspergillus*), lignin (alkali-treated), 5,5-dimethyl-1-pyrroline *N*-oxide (DMPO), quinine sulfate dihydrate ($C_{20}H_{24}N_2O_2{\cdot}H_2SO_4{\cdot}2H_2O$) and ferrous sulfate heptahydrate ($FeSO_4{\cdot}7H_2O$) were purchased from Sigma-Aldrich. $O_2$ (99.999%) and $N_2$ (99.999%) were purchased from US Welding Inc. Deionized (DI) water was used throughout this work.

A Power Research Xenon lamp (ozone-free, 1000 W) for simulated solar irradiation was purchased from Newport Corporation (USA). A standard test sieve (Cole-Parmer Essentials Full Height Sieve, No. 18, 1.00 mm, USA) was used for particle control. Hydrogen peroxide $H_2O_2$ test strips (low level, 0–100 ppm, Bartovation, USA) were applied to determine the concentration of $H_2O_2$ in aqueous samples. A hotplate magnetic stirrer (Thermo Scientific/IKA C-MAG HS 7, USA) was used to stir and/or heat samples.

## 2.2 Fabrication of corn stover-derived CQDs

CQDs were synthesized from corn stover (including stalk, leaf, cob, and husk) using an experimental setup under the illumination of an Xe lamp. A schematic illustration for the experiment is shown in the SI Appendix (Fig. S1). Dried and cleaned corn stover was used as the sole precursor, which was first ground well using a coffee grinder and then sieved through a 1 mm mesh. Corn stover particles with sizes smaller than 1 mm were collected and used for CQD preparation. 0.5 g of corn stover powder was mixed with 100 mL of DI water and transferred into a Teflon-lined stainless-steel autoclave equipped with a quartz window. The reactor was placed on a magnetic stirrer plate and stirred the samples vigorously throughout the reaction. A controlled flow rate of pure oxygen gas was introduced into the reactor, and the reaction temperature was continuously recorded. Vacuum filtration with a 0.22 μm membrane filter was employed to remove the unreacted corn stover powder after the reaction. The residue underwent multiple rinses (2–3 times) using DI water during the filtration process. Subsequently, the liquid sample was subjected to evaporation in a VWR 1330FM mechanical oven (Marshall Scientific, USA) maintained at 50 °C, while maintaining a final CQD solution volume of 100 mL. The obtained CQD solutions were then stored under refrigeration (4 °C) for subsequent experimental applications.

## 2.3 Characterization of CQDs

Three-dimensional excitation emission matrix (3D-EEM) fluorescence was performed using a spectrofluorometer (Fluorolog-3, Horiba, USA), and the photoluminescence property of the CQDs was determined by shifting the excitation wavelengths within 200–600 nm (slits: 4 nm) with an increase of emission wavelengths from 200 to 700 nm (slits: 2 nm). Ultraviolet-visible (UV-vis) absorption spectroscopy was done using a UV-spectrophotometer (Shimadzu). $^1$H-NMR and $^{13}$C-NMR spectra were recorded using a Bruker Avance III 600 MHz spectrometer with deuterium oxide ($D_2O$) as the solvent. Fourier transform infrared (FTIR) spectrum analysis was performed using a spectrophotometer instrument with non-destructive attenuated total reflectance (ATR) technology (Nicolet iS50, Thermo Scientific, USA). The prepared CQDs were scanned 64 times at a resolution of 16 $cm^{-1}$, with a wavenumber range of 4000–400 $cm^{-1}$. X-ray diffraction (XRD) analysis was conducted using an X-ray diffractometer (Rigaku, Japan) with a scanning rate of 4° $min^{-1}$, ranging ($2\theta$) from 10° to 90°. FTIR and XRD were employed to determine the structural characteristics of CQDs. X-ray photoelectron spectroscopy (XPS, Kraros Axis Ultra DLD) was used to determine the surface chemical compositions. ESR spectra were recorded with a Bruker EMX EPR spectrometer (X-band, ~9.87 GHz)

 

using DMPO as a spin trap to detect the measurements (SI Appendix, text S7).

Morphological characterization was carried out using high-resolution transmission electron microscopy (HR-TEM, JEOL JEM-2100F, Japan) with ultra-thin amorphous film-supported copper grids. The elemental composition of the corn stover was determined using a vario MACRO cube elemental analyzer (Elementar), with the oxygen content estimated by the subtraction method (SI Appendix, Table S2). Raman spectra were recorded using a DXR2 Raman spectrometer with a 532 nm excitation laser in the range of 1000–2000 $cm^{-1}$ to analyze the structural characteristics of CQDs. The thermal stability of the samples was determined using a simultaneous thermal analyzer (DSC/TGA SDT Q600). Liquid chromatography-mass spectrometry (LC-MS) analysis was performed using an Agilent 1260 Infinity HPLC system coupled with a 6120 Quadrupole MS equipped with a Hi-Plex H column. Inductively coupled plasma mass spectrometry (ICP-MS) and ion chromatography (IC) analyses were performed using a Thermo iCAP RQ single quadrupole mass spectrometer and a Thermo ICS 6000 system, respectively. A pH meter (Mettler Toledo SevenCompact S220, Switzerland) was used to measure the pH values of the aqueous CQD samples.

### 2.4 Quantum yield measurements

The fluorescence quantum yield (QY) is the ratio of fluorescence photons emitted to excitation photons absorbed. The QYs of the prepared CQDs were evaluated by comparing their integrated photoluminescence (PL) intensities under 340 nm excitation. Quinine sulfate dihydrate in 0.1 M $H_2SO_4$, with a refractive index ($\eta$) of 1.33 and a quantum yield of 0.54 at 350 nm excitation, was used as the standard reference. The CQDs were dissolved in deionized water (refractive index $\eta$ = 1.33) and evaluated at a specific concentration, ensuring that their absorbance value remained below 0.1 at 350 nm. The absorbance at the excitation wavelength of 350 nm was measured using a UV-Vis spectrophotometer (Shimadzu). The photoluminescence emission spectra of the solutions were recorded using a fluorescence spectrometer (Fluorolog-3, Horiba, USA) at an excitation wavelength of 350 nm, with both excitation and emission slit widths set to 2 nm. The integrated PL intensity, representing the total emission within the wavelength range of 300–700 nm, was determined as the area under the PL curve. The QY was calculated using the following equation:[29]

$$QY_{CQDs} = QY_{ST}\left(\frac{A_{CQDs}}{A_{ST}}\right)\left(\frac{I_{ST}}{I_{CQDs}}\right)\left(\frac{{\eta_{CQDs}}^2}{{\eta_{ST}}^2}\right) \quad (1)$$

Here, QY denotes the fluorescence quantum yield, "*A*" represents the measured integrated fluorescence intensity and absorbance, "*I*" denotes the absorbance value, and "$\eta$" refers to the refractive index of the solvent. The subscripts "CQDs" and "ST" denote the aqueous CQD solutions and the standard solution of QS, respectively.

## 3. Results and discussion

### 3.1 Factors affecting CQD synthesis without external $O_2$ introduction

Initial experiments (SI Appendix, Table S1) were conducted to evaluate the feasibility of generating hydrogen peroxide ($H_2O_2$) from water under solar irradiation without the introduction of external oxygen ($O_2$). As shown in SI Appendix (Fig. S1e), $H_2O_2$ accumulated to approximately 50–100 ppm under simulated solar light (>260 nm) within five hours, primarily due to the condensation of water vapor.[26]

Fluorescence and UV-vis spectroscopy analyses (SI Appendix, Fig. S2) revealed that the highest fluorescence intensity was achieved at a light intensity of 834 mW $cm^{-2}$. Further optimization of the reaction duration at this light intensity (SI Appendix, Fig. S3) revealed that 96 h was the optimal duration. The highest-performing sample (Sample 6) exhibited emission peaks at excitation wavelengths of 420–470 nm and 320–370 nm, as characterized by its 3D-EEM fluorescence spectrum (Fig. S3d). The quantum yield of Sample 6 was evaluated as 13.7% (SI Appendix, Table S4).

HRTEM images of Sample 6 revealed CQDs with an average size of 29.8 ± 13.5 nm (Fig. 1a and b). Additionally, larger CQDs (50–100 nm) and irregular carbon sheets with graphite-like structures were observed (Fig. 1c) in the sample. Under UV irradiation (365 nm), the CQDs exhibited blue-green fluorescence (Fig. 1b), despite their size nonuniformity. Their crystal lattice spacing was found to be 0.21 nm, corresponding to the $(1\bar{1}00)$ lattice planes of graphitic carbon, in agreement with prior studies.[3] The UV-vis spectrum (SI Appendix, Fig. S3f) displayed peaks at 232 nm and 278 nm, associated with the $\pi \rightarrow \pi^*$ transition of C═C bonds and the $n \rightarrow \pi^*$ transition of carbonyl groups (C═O), respectively, consistent with previously reported CQDs.

The temperature of the aqueous Sample 6 solution reached ~50 °C at an irradiation intensity of 834 mW $cm^{-2}$ (SI Appendix, Fig. S3f). To distinguish photothermal effects from photocatalytic contributions, a control experiment (SI Appendix, Table S1, Sample 8) was conducted by heating the solution to 50 °C for 96 h in the absence of light (SI Appendix, Fig. S1c). The HRTEM image (Fig. 1d) revealed that Sample 8 contained larger CQDs (69.4 ± 20.5 nm) (Fig. 1e) without graphite-like structures. Although its UV-vis spectrum (Fig. 1f) showed absorption peaks at 232 nm and 280 nm similar to those of Sample 6, its 3D-EEM fluorescence spectrum (Fig. 1g) exhibited significantly lower fluorescence performance than that of Sample 6 (SI Appendix, Fig. S3d). The CQDs from Sample 8 emitted green fluorescence (Fig. 1e), which is attributed to increased particle size heterogeneity. The quantum yield of Sample 8 was 9.0% (SI Appendix, Table S4). These findings suggest that both thermal effects and photocatalytic reactions, particularly $H_2O$-to-$H_2O_2$ conversion, are crucial for CQD formation and optical enhancement.

To further decouple the effects of illumination and oxygen availability, additional control experiments were conducted under dark conditions with $O_2$ (Sample 18) and light con-

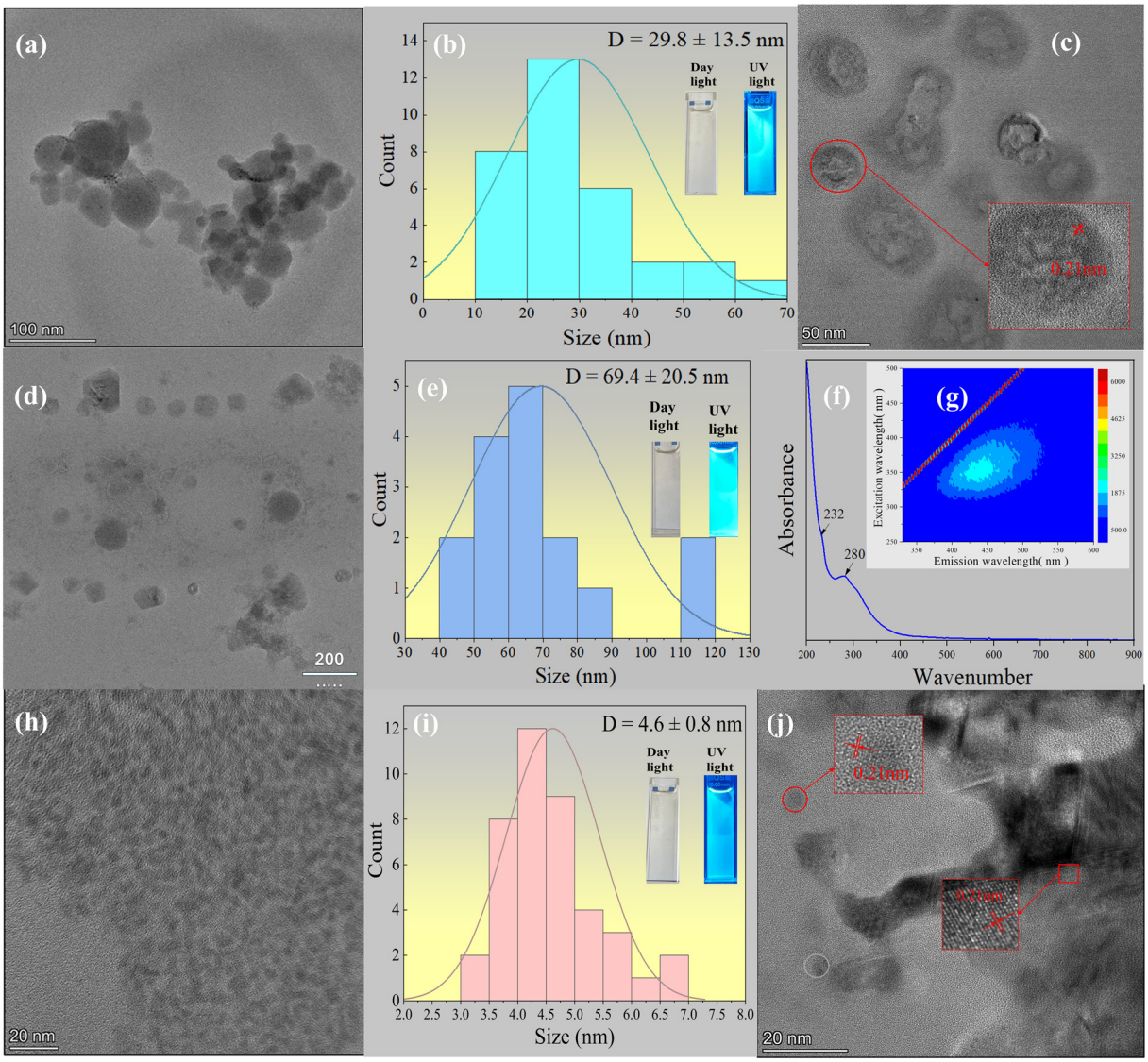


**Fig. 1** (a–c) Characterization of CQDs (Sample 6): (a) HRTEM image showing an amorphous structure (scale bar: 100 nm), (b) size distribution of the CQDs and the photograph of the CQD solution under daylight and a handheld UV flashlight (Alonefire SV003, SVC 365 nm), (c) HRTEM image showing a graphite structure (scale bar: 50 nm); (d–g) characterization of CQDs (Sample 8): (d) TEM image showing an amorphous structure (scale bar: 200 nm), (e) size distribution of the CQDs and the photograph of the CQD solution under daylight and a handheld UV flashlight, (f) UV-vis absorption spectrum, (g) 3D-EEM fluorescence spectrum; (h and i) characterization of CQDs (Sample 10): (h) HRTEM image showing an amorphous structure (scale bar: 20 nm), (i) size distribution of the CQDs and the photograph of the CQD solution under daylight and a handheld UV flashlight; (j) HRTEM image showing a graphite structure including a zoomed-in view (scale bar: 20 nm).

ditions with $N_2$ (Sample 19), which are described in Text S6 and Fig. S7. Through their 3D-EEM results, almost no fluorescence (Fig. S7a) was observed in Sample 18, demonstrating that oxygen alone—without illumination-driven interfacial activation—is difficult to generate detectable amounts of CQDs. Conversely, illumination in the absence of a continuous oxygen supply (light with $N_2$, Sample 19) produced CQDs with quite weak fluorescence (Fig. S7b) due to the $O_2$-deficient environment. When considered together with light with the atmospheric environment (Sample 6), light with the $O_2$-rich environment (Sample 10), and dark with external heating (Sample 8) experiments, these results confirm that both illumination and oxygen are simultaneously required for high efficiency of CQD formation.

### 3.2 Factors affecting CQD synthesis with external $O_2$ introduction

Additional experiments were conducted with $O_2$ introduction to synthesize uniform, high-performance CQDs. The effect of $O_2$ flow rate on CQD synthesis was investigated (SI Appendix, Table S1, Samples 9–11). The results (SI Appendix, Fig. S4) show that Sample 10, synthesized at an $O_2$ flow rate of 28 mL $min^{-1}$, exhibited optimal fluorescence performance. HRTEM images of Sample 10 (Fig. 1h and i) revealed a monodisperse

CQD population with an average diameter of 4.6 ± 0.8 nm. In addition, graphite sheets and some graphite-like quantum dots (5–10 nm) were observed with a lattice spacing of 0.21 nm (Fig. 1j), consistent with those observed in Sample 6 (Fig. 1c). Notably, the quantum yield of Sample 10 reached 20.1 ± 0.8% (SI Appendix, Table S4), which is more than double that of Sample 8 (9.0%) synthesized under dark conditions with external heating at the same temperature.

The structural characterization of CQDs (Sample 10) synthesized under $O_2$-rich conditions was performed using XRD, ATR-FTIR, Raman spectroscopy, NMR, and XPS. The XRD pattern (Fig. 2a) exhibits a broad diffraction peak at 21°, corresponding to the (002) plane of amorphous graphite (JCPDS: 41-1487), indicating low graphitization.[30] ATR-FTIR spectra (Fig. 2b) showed characteristic functional groups, including O–H/N–H (3500–3000 $cm^{-1}$), C–H (2930 $cm^{-1}$), C═C (1580 $cm^{-1}$), C–O (1243 $cm^{-1}$), and C═O (1690–1740 $cm^{-1}$).[31–34] The obtained Raman spectrum (Fig. 2c) was baseline-corrected and fitted using Gauss functions, revealing the characteristic D band (~1348 $cm^{-1}$) and G band (~1573 $cm^{-1}$) associated with disordered and graphitic $sp^2$ carbon, respectively. An $I_D/I_G$ ratio of 1.4, calculated based on the integrated peak areas of the fitted bands, indicates a high level of structural disorder relative to the graphitic content.[35]

NMR spectroscopy (Fig. 2d and e) shows proton signals at 1–3 ppm ($sp^3$ C–H), 3–6 ppm (oxygenated groups), and 8–10 ppm (aldehydic protons). The $^{13}C$ NMR spectrum displays signals at 20–80 ppm ($sp^3$ carbon), 80–100 ppm (ether-bound carbon), 100–120 ppm (aromatic carbon), and 170–185 ppm (carboxyl or ester C═O).[36,37] XPS analysis (Fig. 2f–i) indicates peaks corresponding to C–C/C═C, C–O/C–N, and C═O in the C 1s spectrum, while O 1s/N 1s spectra confirmed the presence of oxygen-containing functionalities and pyridinic-N/amide-N species.

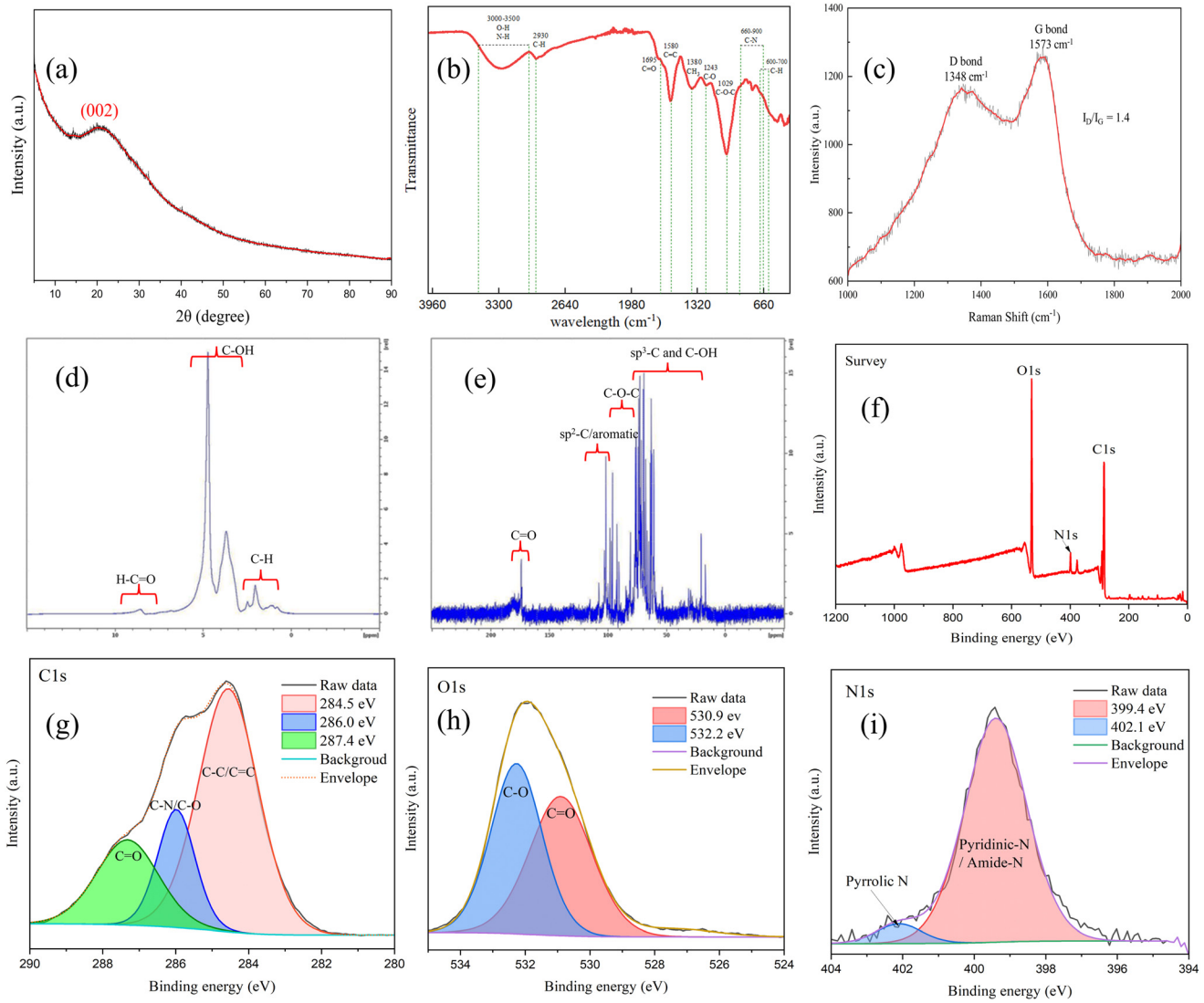


**Fig. 2** The structural analysis of the CQDs (Sample 10): (a) XRD patterns; (b) ATR-FTIR spectrum; (c) Raman spectrum; (d) $^1H$ NMR spectrum; (e) $^{13}C$ NMR spectrum; XPS spectrum survey scan (f) and corresponding expansion for (g) C 1s, (h) O 1s and (i) N 1s peaks of the CQDs.

These results highlight the synergistic roles of $O_2$ in photothermal and photocatalytic processes, leading to the formation of smaller, more uniform CQDs with enhanced fluorescence. The self-doping of nitrogen from corn stover contributed to a high quantum yield (20.1 ± 0.8%), demonstrating an efficient and sustainable approach to CQD synthesis.[12]

To obtain high-purity CQDs, centrifugation and dialysis were employed (Sample 10) as described in SI Appendix (Text S10). The purity of the CQDs was then evaluated using multiple analytical techniques, including LC-MS, ICP-MS, and IC to detect residual small molecules, metal ions, and anionic species (SI Appendix, Text S11). Fig. 3 presents the comprehensive characterization of CQDs after purification by centrifugation and dialysis. HRTEM images (Fig. 3a and f) reveal that the CQDs are uniformly dispersed, with average diameters of 3.1 ± 1.4 nm and 3.7 ± 1.6 nm, respectively, confirming good size uniformity and monodispersity. The high-resolution image in Fig. 3d shows clear lattice fringes with an interplanar spacing of 0.21 nm, corresponding to the (100) plane of graphitic carbon,[2] further supported by the FFT patterns in Fig. 3b and e, indicating partial crystallinity. The 3D-EEM spectrum (Fig. 3c) and accompanying photographs demonstrate strong fluorescence and excel-

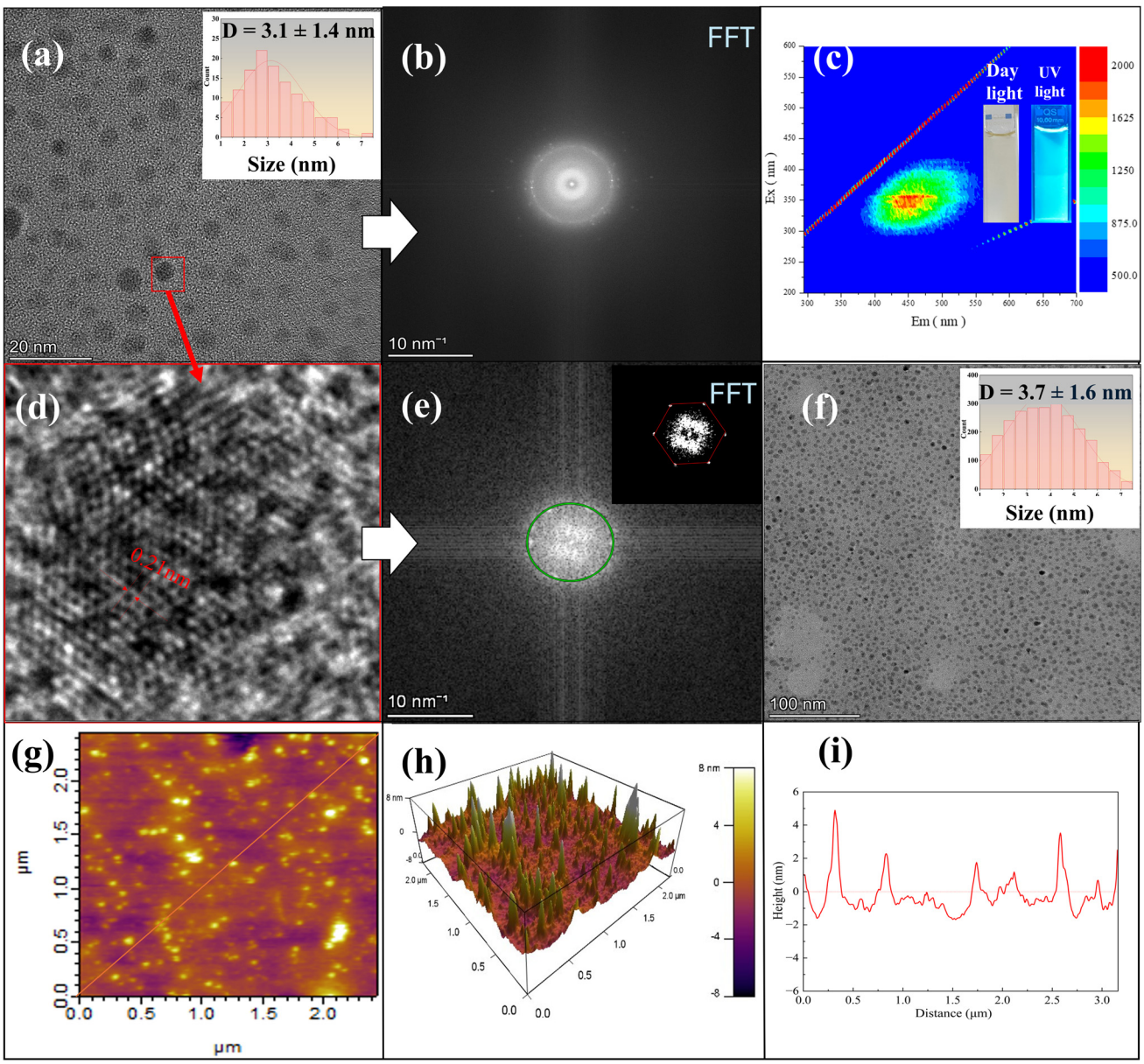


**Fig. 3** CQDs (Sample 10) after dialysis filtration: (a) HRTEM image and size distribution (scale bar: 20 nm); (b) fast Fourier transform (FFT) pattern corresponding to (a); (c) 3D-EEM fluorescence spectrum and the photograph of the CQD solution under daylight and a handheld UV flashlight (Alonefire SV003, SVC 365 nm); (d) HRTEM image of the CQDs indicating a lattice spacing; (e) FFT pattern corresponding to (d); (f) HRTEM image and size distribution (scale bar: 100 nm); and (g–i) AFM images of 2D, 3D, and the corresponding height-profile along the marked line in (g).

Table 1 Summary of key synthesis conditions and representative properties of CQDs prepared under different reaction conditions

| Sample | Key conditions | Particle size (nm) | Quantum yield (%) |
|---|---|---|---|
| Sample 6 | Light: 834 mW $cm^{-2}$; atmospheric environment; 96 h | 29.8 ± 13.5 | 13.7 |
| Sample 8 | Dark; heating to 50 °C; atmospheric environment; 96 h | 69.4 ± 20.5 | 9.0 |
| Sample 10 | Light: 834 mW $cm^{-2}$; rich-$O_2$; 96 h | 4.6 ± 0.8 (after dialysis: 3.1 ± 0.4) | 20.1 ± 0.8 |

lent optical properties of the CQDs under UV light. AFM analysis (Fig. 3g–i) further confirms the nanoscale size and uniform height distribution of individual CQDs, with a height range of ~3–4 nm and no visible aggregation. TEM analysis (SI Appendix, Fig. S12) of multiple regions confirms that the carbon quantum dots (CQDs) exhibit diameters ranging from approximately 3 to 4 nm, demonstrating that dialysis successfully yielded well-dispersed individual nanoparticles with no observable aggregation. These results confirm that centrifugation and dialysis effectively remove impurities while preserving the structural integrity, size uniformity, and fluorescence properties of the CQDs.

The key synthesis conditions, particle sizes, and quantum yields of representative samples are summarized in Table 1. To clarify how structural features govern photoluminescence (PL), we quantitatively compared particle size, surface chemistry, and graphitic domain structure across samples. TEM analysis (Fig. 1 and 2d) shows that CQDs synthesized under light + rich-$O_2$ (Sample 10) are the smallest (4.6 ± 0.8 nm before purification; 3.1 ± 0.4 nm after dialysis), whereas the oxygen-limited condition (Sample 6) produces much larger particles (29.8 ± 13.5 nm), and the dark–thermal condition (Sample 8) yields even larger amorphous structures (69.4 ± 20.5 nm). Correspondingly, Sample 10 exhibits the strongest PL emission (Fig. S2–S5), consistent with quantum confinement, while samples forming larger particles show weaker and broader emission. FTIR and XPS analyses (Fig. 2b and f–i) indicate that Sample 10 contains abundant oxygen-containing functional groups (C═O, C–OH, and epoxy), which are known to create radiative surface states that can enhance PL. Raman spectroscopy (Fig. 2c) further shows an $I_D/I_G$ ratio of 1.4 for Sample 10, indicating defect-rich $sp^2$ nanodomains that are also associated with emissive sites. Together, these results demonstrate that bright PL arises from the combined effects of ultrasmall particle size, oxygen-rich surface states, and defect-engineered $sp^2$ domains formed uniquely under simultaneous illumination and $O_2$ supply.

### 3.3 Formation of CQDs from corn stover

The mechanism of CQD formation from natural biomass remains incompletely established.[38] In this study, we propose a pathway involving photothermal and photocatalytic oxidation of lignin, hemicellulose, and cellulose in corn stover, primarily driven by Fenton and Fenton-like reactions. This reaction employs *in situ*-generated $H_2O_2$ (SI Appendix, Fig. S1e) and naturally occurring metal ions (SI Appendix, Table S3). The system utilizes an ozone-free xenon lamp, ensuring that unwanted UV wavelengths (<260 nm) are filtered out to prevent ozone formation and associated side reactions.

**3.3.1 $H_2O_2$ generation at water interfaces.** Conventional $H_2O_2$ production typically requires $H_2O$, $O_2$, and photocatalysts under UV or solar irradiation.[39,40] In contrast, we demonstrate that interfacial water microenvironments formed by vaporization at the water–air interface can spontaneously and continuously generate $H_2O_2$ under simulated solar irradiation, without the need for additional catalysts. This phenomenon aligns with the interfacial charge-transfer mechanism reported previously:[24]

$$H_2O \rightarrow H^+ + OH^- \quad (R1)$$

$$OH^- \rightarrow {}^{\bullet}OH + e^- \quad (R2)$$

$${}^{\bullet}OH + {}^{\bullet}OH \rightarrow H_2O_2 \quad (R3)$$

Another mechanism is electron transfer from $OH^-$ to $H^+$ at the interface, followed by $^{\bullet}OH$ radical recombination, while both $^{\bullet}OH$ and $^{\bullet}H$ have been detected experimentally using electron spin resonance (ESR) spectroscopy.[41] In addition, contact electrification at the water–solid interface[42,43] has been reported to contribute to $H_2O_2$ formation.

In the present system, elevated solution temperatures (~50 °C) under illumination lead to partial water vaporization, followed by continuous condensation at the water–air interface, enabling continuous $H_2O_2$ generation (Fig. 4a). $H_2O_2$ formation is further enhanced by UV radiation,[44] as confirmed using $H_2O_2$ test strips (0–100 ppm) (SI Appendix, Fig. S1d).

Building on the foundational discovery that $H_2O$ at the hydrophilic–hydrophobic interface yields $H_2O_2$,[24,25] our approach further integrates simulated solar light to further enhance $H_2O_2$ production through photochemical pathways. This strategy synergistically couples interfacial electrochemical processes with photochemical activation, enabling sustained $H_2O_2$ generation without the need for external catalysts or energy-intensive UV sources, supporting a scalable and sustainable reaction pathway.

**3.3.2 Acid leaching of metal ions from corn stover.** Protons ($H^+$) and hydrogen atoms ($^{\bullet}H$) generated in this system facilitate the leaching of metal ions from corn stover into the aqueous phase. ICP-MS analysis (SI Appendix, Table S3) detected a concentration of 0.81 ppm ($Fe^{2+}/Fe^{3+}$) in the CQD solution, confirming effective metal ion dissolution. The resulting Fenton reaction proceeds at a bulk solution pH of 5.02, although localized pH values near reactive interfaces may be lower during the reaction.

**3.3.3 Fenton and Fenton-like reactions.** The classical Fenton process involves the following reactions:[45]

$$Fe^{2+} + H_2O_2 \rightarrow Fe^{3+} + {}^{\bullet}OH + OH^- \quad (R4)$$

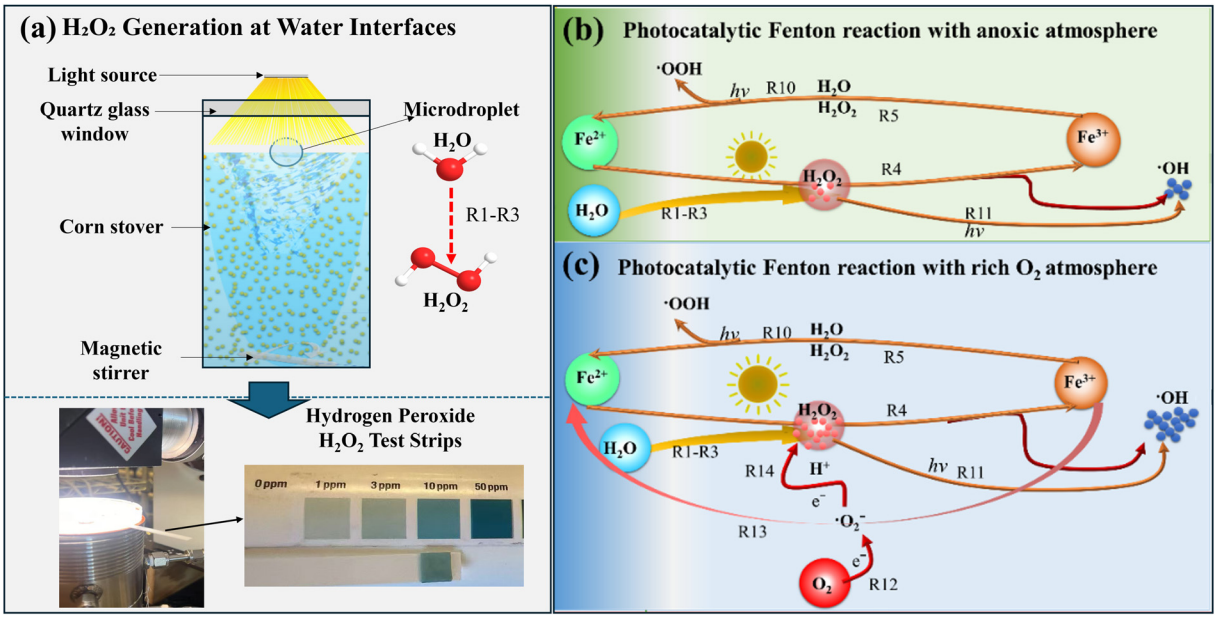


**Fig. 4** Proposed mechanism of peroxide generation and localized radical activation under illumination conditions.

$$Fe^{3+} + H_2O_2 \rightarrow Fe^{2+} + {}^{\bullet}OOH + H^+ \quad (R5)$$

$$Fe^{2+} + {}^{\bullet}OH \rightarrow Fe^{3+} + OH^- \quad (R6)$$

$$H_2O_2 + {}^{\bullet}OH \rightarrow {}^{\bullet}OOH + H_2O \quad (R7)$$

$$Fe^{2+} + {}^{\bullet}OOH + H^+ \rightarrow Fe^{3+} + H_2O_2 \quad (R8)$$

$$Fe^{3+} + {}^{\bullet}OOH \rightarrow Fe^{2+} + O_2 + H^+ \quad (R9)$$

Hydroxyl radicals ($^{\bullet}OH$) generated through these reactions oxidatively degrade organic molecules in corn stover, facilitating CQD formation. In addition to iron, other multivalent metal ions (*e.g.*, Co, Cr, Cu, Mn, Mo, Ru, Ti, W, and V), detected by ICP-MS (SI Appendix, Table S3), may participate in Fenton-like reactions, further contributing to reactive oxygen species generation.[46]

Simulated solar irradiation enhances the Fenton process through photo-induced reactions (Fig. 4b),[47] as described using the following equations:

$$Fe^{3+} + H_2O + h\nu \rightarrow Fe^{2+} + {}^{\bullet}OH + H^+ \quad (R10)$$

$$H_2O_2 + h\nu \rightarrow {}^{\bullet}OH + {}^{\bullet}OH \quad (R11)$$

These reactions continuously regenerate $Fe^{2+}$ and produce additional $^{\bullet}OH$ radicals, accelerating oxidative degradation. Experimental results confirm that UV light (250–430 nm) plays a crucial role in CQD synthesis, as evidenced by increased fluorescence intensity and reduced pH, indicating enhanced formation of organic acids (–COOH) during biomass degradation (SI Appendix, Fig. S5 and Table S1).

Molecular oxygen further promotes $Fe^{3+}$ reduction and reactive oxygen species (ROS) generation,[48] as illustrated by the following reactions:

$$e^- + O_2 \rightarrow {}^{\bullet}O_2^- \quad (R12)$$

$$Fe^{3+} + {}^{\bullet}O_2^- \rightarrow Fe^{2+} + O_2 \quad (R13)$$

$$^{\bullet}O_2^- + e^- + 2H^+ \rightarrow H_2O_2 \quad (R14)$$

The resulting superoxide radicals ($^{\bullet}O_2^-$) react with $H_2O$ to form additional $H_2O_2$, accelerating the photo-Fenton cycle.[49] An $O_2$-rich atmosphere consequently enhances the oxidative degradation of hemicellulose, cellulose, and lignin, boosting CQD yield (Fig. 4c). In parallel, organic radical intermediates may undergo peroxo-organic transformations,[50,51] further amplifying oxidative pathways and promoting CQD formation.

ESR spin-trapping experiments were carried out to detect ROS formation and peroxide accumulation using DMPO (SI Appendix, Fig. S8). Fig. S8a exhibits a four-line ESR pattern of $H_2O_2$ standards measured with $Fe^{2+}$ triggering. In biomass-free controls (Fig. S8b), illumination and $O_2$ flow induce discernible ESR signals absent under dark conditions, indicating interfacial photochemical radical generation, although the spectra are broadened by overlapping ROS adducts. In the corn-stover-containing system (Fig. S8c), ESR signals are weak and broadened due to the rapid radical consumption and heterogeneous scavenging by biomass-derived organic species and redox-active sites. Notably, $Fe^{2+}$ addition at extended reaction time (60 min) markedly enhances the ESR response, supporting the accumulation of peroxide species and their involvement in localized, transient radical activation during CQD formation.

### 3.4 Corn stover conversion to CQDs

Corn stover primarily consists of cellulose (35–40%), hemicellulose (20–25%), lignin (19–22%) and trace metals (*e.g.*, $Fe^{2+}$).[52] Control experiments using isolated cellulose, hemi-

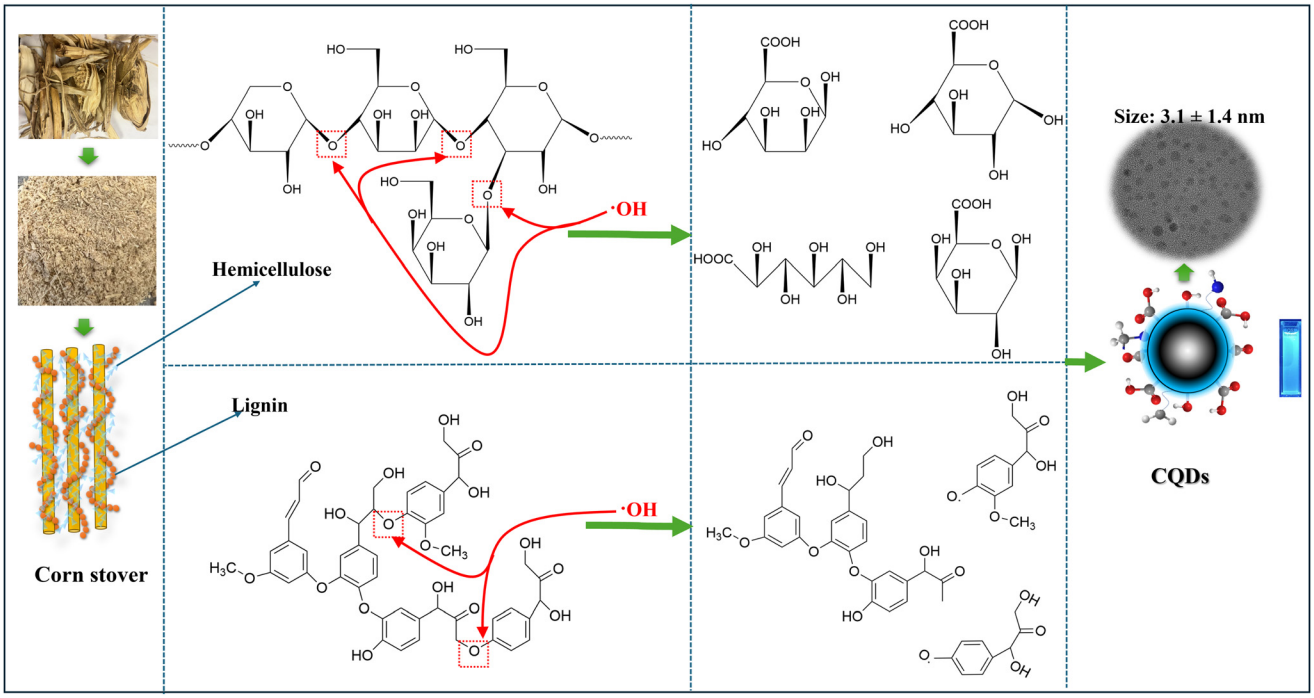


**Fig. 5** Proposed pathway for CQD formation from corn stover *via* peroxide-mediated oxidative depolymerization.

cellulose, and lignin as individual precursors yielded markedly weaker fluorescence under identical reaction conditions (SI Appendix, Fig. S6), displaying that hemicellulose and lignin can be easily degraded and contribute to CQD production.

Hemicellulose, a heteropolymer of sugars (xylan and glucan), and lignin, a complex phenylpropanoid network, undergo preferential oxidative degradation in this system, while the proposed pathway of CQD production is shown in Fig. 5. Hydroxyl radicals (˙OH) cleave glycosidic (C–O–C) linkages in polysaccharides and β-O-4 ether bonds, fragmenting these macromolecules into monomeric and oligomeric sugars as well as phenolic compounds (*e.g.*, vanillin, syringol, and guaiacol).[53,54] Notably, as-formed CQDs may enhance Fenton reactions by acting as photocatalysts, promoting ˙OH radical production.[55–57] Their surface carboxyl functional groups can lower the solution pH, thereby optimizing the reaction efficiency.[54] Consistent with this interpretation, the solution pH decreased with prolonged reaction time and higher $O_2$ flow rates, reaching 4.09 under $O_2$-rich conditions (SI Appendix, Table S1, Sample 10), indicating enhanced organic acid formation and controlled $H_2O_2$ consumption.

### 3.5 Comparison with conventional CQD synthesis methods

For comparison, Tables S6–S8 systematically evaluate the reported CQD synthesis methods in terms of raw materials, reaction conditions, CQD sizes, quantum yields, and environmental considerations.

Table S6 shows a comparison of CQD synthesis routes involving high-temperature pyrolysis (≥300 °C), two-step carbonization, or hydrothermal methods with added chemicals. These methods often require elevated temperatures (300–700 °C) or strong acids, bases, or oxidants, which can complicate purification and introduce secondary environmental burdens, despite achieving high quantum yields in some cases. Table S7 focuses on one-step hydrothermal and photothermal CQD synthesis using only biomass and water. Compared with hydrothermal processes reported by other groups, the present photothermal method operates at substantially lower temperatures, requires less stringent equipment, and produces fewer liquid organic byproducts, resulting in easier CQD separation and higher product purity. Although several hydrothermal studies report higher quantum yields, these typically rely on higher temperatures or fresh biomass sources rich in soluble carbon, which are more readily degraded than solid lignocellulosic feedstocks. Table S8 shows a comparison of CQD synthesis strategies based on externally added $H_2O_2$ and catalysts with those relying on internally generated $H_2O_2$. In contrast to methods requiring large $H_2O_2$ dosages and added catalysts (*e.g.*, $Fe^{2+}/Fe^{3+}$ or $W_{18}O_{49}$), the present approach generates $H_2O_2$ *in situ* without external oxidants or catalysts. This eliminates the need for costly reagents, reduces overoxidation of carbon precursors, enables smaller CQD sizes, and lowers overall energy demand due to the mild reaction temperature.

Overall, this work demonstrates a green and economically attractive CQD synthesis route that combines renewable biomass, internally generated oxidants, ambient-pressure operation, and low thermal input, offering clear advantages over conventional high-temperature or chemically intensive methods.

## 4. Conclusions

This CQD synthesis strategy minimizes byproducts, simplifies purification, and eliminates harsh acids (*e.g.*, $H_2SO_4$ and $HNO_3$). By leveraging corn stover as both a carbon source and a natural catalytic reservoir, it efficiently integrates spontaneous $H_2O$-to-$H_2O_2$ conversion under solar irradiation, providing an environmentally sustainable route for high-purity CQD production. These results extend microdroplet chemistry into the realm of biomass valorization and highlight a sustainable, external-catalyst-free strategy for converting raw biomass into high-quality nanocarbon materials.

## Author contributions

M. Fan, X. Kang, and R. N. Zare designed the research concepts; X. Kang performed the major research tasks, including tests and data analyses, and prepared the initial draft of the manuscript. Q. Yang, S. X. Tang, Z. Chen, S. Budhathoki, R. Paneru, S. Kim and A. Goroncy assisted X. Kang in performing the research tasks. Y. Bai, Qian Li, and Z. Chen assisted M. Fan, X. Kang, and R. N. Zare in developing the research concepts. X. Kang, M. Fan, and R. N. Zare worked together to finalize the manuscript.

## Conflicts of interest

The authors declare no conflicts of interest.

## Data availability

All data supporting the findings of this study are available within the paper and its supplementary information (SI). Supplementary information: Text S1–S11, Fig. S1–S12 and Tables S1–S8 provide additional experimental details and analyses, including the effects of light intensity, reaction time, oxygen flow, light wavelength ranges, and separated corn stover components, as well as descriptions of Fenton and Fenton-like reactions, thermogravimetric analysis, ESR spectra, and purification protocols with purity evaluation. Characterization data (TEM, 3D-EEM, TGA, LC-MS, ICP-MS, IC, and pH), together with tables containing comparisons to conventional CQD synthesis methods as well as their reported quantum yields of CQDs, are also provided. See DOI: https://doi.org/10.1039/d5gc04545b.

## Acknowledgements

We would like to thank Zhaojie Zhang for the help with fluorescence microscopy measurements. This work was supported by the University of Wyoming and the Czech University of Life Sciences Prague.

## References

1 S. Y. Lim, W. Shen and Z. Gao, *Chem. Soc. Rev.*, 2015, **44**, 362–381.
2 W. Li, W. Zhou, Z. Zhou, H. Zhang, X. Zhang, J. Zhuang, Y. Liu, B. Lei and C. Hu, *Angew. Chem., Int. Ed.*, 2019, **131**, 7356–7361.
3 L. Wang, W. Li, L. Yin, Y. Liu, H. Guo, J. Lai, Y. Han, G. Li, M. Li, J. Zhang, R. Vajtai, P. M. Ajayan and M. Wu, *Sci. Adv.*, 2020, **6**, eabb6772.
4 Y. Li, X. Zhang, W. Hou, Z. Zhou, S. Zhang, H. Guo, J. Zhang, J. Xu and L. Wang, *Appl. Catal., B*, 2026, **380**, 125758.
5 X. Xu, R. Ray, Y. Gu, H. J. Ploehn, L. Gearheart, K. Raker and W. A. Scrivens, *J. Am. Chem. Soc.*, 2004, **126**, 12736–12737.
6 R. Liu, D. Wu, S. Liu, K. Koynov, W. Knoll and Q. Li, *Angew. Chem., Int. Ed.*, 2009, **48**, 4598–4601.
7 L. Cao, X. Wang, M. J. Meziani, F. Lu, H. Wang, P. G. Luo, Y. Lin, B. A. Harruff, L. M. Veca, D. Murray, S. Y. Xie and Y. P. Sun, *J. Am. Chem. Soc.*, 2007, **129**, 11318–11319.
8 A. Xu, G. Wang, Y. Li, H. Dong, S. Yang, P. He and G. Ding, *Small*, 2020, **16**, 2004621.
9 S. Chen, S. Z. Zhang and H. Jiang, *ACS ES&T Water*, 2024, **4**, 531–542.
10 S. N. Baker and G. A. Baker, *Angew. Chem., Int. Ed.*, 2010, **49**, 6726–6744.
11 S. Chung, R. A. Revia and M. Zhang, *Adv. Mater.*, 2021, **33**, 1904362.
12 R. Paneru, X. Kang, S. Budhathoki, Z. Chen, Q. Yang, S. T. Tjeng, Q. Dai, W. Wang, J. Tang and M. Fan, *J. Environ. Sci.*, 2025, **154**, 590–601.
13 H. Ding, S. B. Yu, J. S. Wei and H. M. Xiong, *ACS Nano*, 2016, **10**, 484–491.
14 B. Dutcher, M. Fan, B. Leonard, M. D. Dyar, J. Tang, E. A. Speicher, P. Liu and Y. Zhang, *J. Phys. Chem. C*, 2011, **115**, 15532–15544.
15 M. Yang, L. Guo, G. Hu, X. Hu, J. Chen, S. Shen, W. Dai and M. Fan, *Ind. Eng. Chem. Res.*, 2016, **55**, 757–765.
16 P. M. Gawal and A. K. Golder, *Colloids Surf., A*, 2024, **683**, 133068.
17 T. J. Pillar-Little, N. Wanninayake, L. Nease, D. K. Heidary, E. C. Glazer and D. Y. Kim, *Carbon*, 2018, **140**, 616–623.
18 D. Xu, C. Yu, X. Peng, H. Yan and Y. Zhang, *Res. Chem. Intermed.*, 2024, **50**, 4597–4617.
19 V. G. Matveeva and L. M. Bronstein, *Prog. Mater. Sci.*, 2022, **130**, 100999.
20 S. C. Perry, D. Pangotra, L. Vieira, L. I. Csepei, V. Sieber, L. Wang, C. Ponce de León and F. C. Walsh, *Nat. Rev. Chem.*, 2019, **3**, 442–458.
21 X. Zhou, Y. Zhang, C. Wang, X. Wu, Y. Yang, B. Zheng, H. Wu, S. Guo and J. Zhang, *ACS Nano*, 2012, **6**, 6592–6599.
22 C. Zhu, S. Yang, G. Wang, R. Mo, P. He, J. Sun, Z. Di, Z. Kang, N. Yuan, J. Ding, G. Ding and X. Xie, *J. Mater. Chem. B*, 2015, **3**, 6871–6876.

 

23 D. Y. Lee, Z. Haider, S. K. Krishnan, T. Kanagaraj, S. H. Son, J. Jae, J. R. Kim, P. S. M. Kumar and H. I. Kim, *Chemosphere*, 2024, **361**, 142330.
24 M. A. Mehrgardi, M. Mofidfar and R. N. Zare, *J. Am. Chem. Soc.*, 2022, **144**, 7606–7609.
25 J. K. Lee, K. L. Walker, H. S. Han, J. Kang, F. B. Prinz, R. M. Waymouth, H. G. Nam and R. N. Zare, *Proc. Natl. Acad. Sci. U. S. A.*, 2019, **116**, 19294–19298.
26 J. K. Lee, H. S. Han, S. Chaikasetsin, D. P. Marron, R. M. Waymouth, F. B. Prinz and R. N. Zare, *Proc. Natl. Acad. Sci. U. S. A.*, 2020, **117**, 30934–30941.
27 X. Song, C. Basheer, J. Xu and R. N. Zare, *Sci. Adv.*, 2024, **10**, 4443.
28 Y. Meng, Y. Xia, J. Xu and R. N. Zare, *Sci. Adv.*, 2025, **11**, 8979.
29 H. Kalita, J. Mohapatra, L. Pradhan, A. Mitra, D. Bahadur and M. Aslam, *RSC Adv.*, 2016, **6**, 23518–23524.
30 A. Afzalalghom, A. Beitollahi, S. M. Mirkazemi, M. Maleki and H. Sarpoolaky, *Small*, 2024, **20**, 2308082.
31 B. Al-Hashimi, K. M. Omer and H. S. Rahman, *Arabian J. Chem.*, 2020, **13**, 5151–5159.
32 N. B. Mandava, in *Handbook of Natural Pesticides: Methods*, CRC Press, 2019, pp. 219–256.
33 H. Nie, M. Li, Q. Li, S. Liang, Y. Tan, L. Sheng, W. Shi and S. X. A. Zhang, *Chem. Mater.*, 2014, **26**, 3104–3112.
34 S. Moonrinta, B. Kwon, I. In, S. Kladsomboon, W. Sajomsang and P. Paoprasert, *Opt. Mater.*, 2018, **81**, 93–101.
35 A. C. Ferrari and D. M. Basko, *Nat. Nanotechnol.*, 2013, **8**, 235–246.
36 S. Zhu, Q. Meng, L. Wang, J. Zhang, Y. Song, H. Jin, K. Zhang, H. Sun, H. Wang and B. Yang, *Angew. Chem., Int. Ed.*, 2013, **52**, 4045–4049.
37 B. De and N. Karak, *RSC Adv.*, 2013, **3**, 8286–8290.
38 M. Si, J. Zhang, Y. He, Z. Yang, X. Yan, M. Liu, S. Zhuo, S. Wang, X. Min, C. Gao, L. Chai and Y. Shi, *Green Chem.*, 2018, **20**, 3414–3419.
39 C. Pan, G. Bian, Y. Zhang, Y. Lou, Y. Zhang, Y. Dong, J. Xu and Y. Zhu, *Appl. Catal., B*, 2022, **316**, 121675.
40 T. Liu, Z. Pan, J. J. M. Vequizo, K. Kato, B. Wu, A. Yamakata, K. Katayama, B. Chen, C. Chu and K. Domen, *Nat. Commun.*, 2022, **13**, 1034.
41 J. Li, Y. Xia, X. Song, B. Chen and R. N. Zare, *Proc. Natl. Acad. Sci. U. S. A.*, 2024, **121**, e2318408121.
42 A. Gallo Jr., N. H. Musskopf, X. Liu, Z. Yang, J. Petry, P. Zhang, S. Thoroddsen, H. Im and H. Mishra, *Chem. Sci.*, 2022, **13**, 2574–2583.
43 B. Chen, Y. Xia, R. He, H. Sang, W. Zhang, J. Li, L. Chen, P. Wang, S. Guo, Y. Yin, L. Hu, M. Song, Y. Liang, Y. Wang, G. Jiang and R. N. Zare, *Proc. Natl. Acad. Sci. U. S. A.*, 2022, **119**, e2209056119.
44 B. C. Faust, C. Anastasio, J. M. Allen and T. Arakaki, *Science*, 1993, **260**, 73–75.
45 J. De Laat and H. Gallard, *Environ. Sci. Technol.*, 1999, **33**, 2726–2732.
46 Y. Liu and J. Wang, *Chem. Eng. J.*, 2023, **466**, 143147.
47 J. Kiwi, C. Pulgarin and P. Peringer, *Appl. Catal., B*, 1994, **3**, 143147.
48 S. Chen, Y. Chen, Y. Zhang, X. Kuang, Y. Liu, M. Guo, L. Ma, D. Zhang and Q. Li, *Front. Neurosci.*, 2020, **14**, 601193.
49 P. Zhou, J. Xu, J. Guo, X. Hou, L. Dai, X. Xiao and K. Huo, *Green Chem.*, 2024, **26**, 6005–6018.
50 O. Legrini, E. Oliveros and A. M. Braun, *Chem. Rev.*, 1993, **93**, 671–698.
51 B. Utset, J. Garcia, J. Casado, X. Domènech and J. Peral, *Chemosphere*, 2000, **41**, 1187–1192.
52 A. H. Rony, L. Kong, W. Lu, M. Dejam, H. Adidharma, K. A. M. Gasem, Y. Zheng, U. Norton and M. Fan, *Bioresour. Technol.*, 2019, **284**, 466–473.
53 D. Van Eylen, F. van Dongen, M. Kabel and J. de Bont, *Bioresour. Technol.*, 2011, **102**, 5995–6004.
54 E. Mnich, N. Bjarnholt, A. Eudes, J. Harholt, C. Holland, B. Jørgensen, F. H. Larsen, M. Liu, R. Manat, A. S. Meyer, J. D. Mikkelsen, M. S. Motawia, J. Muschiol, B. L. Møller, S. R. Møller, A. Perzon, B. L. Petersen, J. L. Ravn and P. Ulvskov, *Nat. Prod. Rep.*, 2020, **37**, 919–961.
55 T. Zhang, Y. Wen, Z. Pan, Y. Kuwahara, K. Mori, H. Yamashita, Y. Zhao and X. Qian, *Environ. Sci. Technol.*, 2022, **56**, 2617–2625.
56 Y. Yang, Q. Guo, Q. Li, L. Guo, H. Chu, L. Liao, X. Wang, Z. Li and W. Zhou, *Adv. Funct. Mater.*, 2024, **34**, 2400612.
57 W. Han, H. Zhang, D. Li, W. Qin, X. Zhang, S. Wang and X. Duan, *Appl. Catal., B*, 2024, **350**, 123918.